Electronic Supplementary Material

An advanced necklace-like metal organic framework with an ultrahighly continuous structure in the membrane for superior butanol/water separation

Li-Hao Xu, Shen-Hui Li, Heng Mao, Ao-Shuai Zhang, Wei-Wei Cai, Tao Wang, Zhi-Ping Zhao*

School of Chemistry and Chemical Engineering, Beijing Institute of Technology,

Beijing 102488, P. R. China

E-mail: zhaozp@bit.edu.cn

Materials and chemicals

Pyrrole, methyl orange (MO), ferric chloride anhydrous ($FeCl_3$), and *n*-butanol were purchased from Shanghai Macklin Biochemical Technology co., Ltd (China). Zinc nitrate hexahydrate ($Zn(NO_3)_2 \cdot 6H_2O$), 2-methylimidazole (2-MeIm), tetraethyl orthosilicate (TEOS), dibutyltin dilaurate (DBTDL), diiodomethane, glycerine and *n*-heptane were purchased from Shanghai Aladdin Biochemical Technology co., Ltd (China). Hydroxyl-terminated PDMS (viscosity, 20000 mPa·s) was supplied by Jinan Xingchi Chemical co., Ltd (China). Polyvinylidene fluoride (PVDF) substrate membrane was produced by using the equipment of Dalian Kena co., Ltd (China). Other solvents were obtained from Beijing Chemical Works (China). All reagents were used without further purification.

Characterization of ZIF-8@PPy powder and membranes

The morphologies of the nanomaterials and various membrane samples were observed using a ZEISS SUPRA™ 55 field-emission scanning electron microscope (FESEM, Germany) operated at 10 kV. Coupled with SEM, the energy-dispersive X-ray spectrometry (EDXS) allowed elemental mapping of the MOFs necklaces, and the scanning time was 180 s. Before SEM testing, the cross-sections of the membranes were freeze-fractured in liquid nitrogen, and all samples were sprayed with Au for 90 s using an auto fine coater (JEOL JFC-1600, Japan) operating at 23 mA, under a vacuum pressure to ensure high conductivity. High-resolution transmission electron microscopy (HR-TEM, JEOL JEM-2100, Japan, operating at an accelerating voltage of 200 kV) images were obtained to observe the morphology and structure of the PPy nanotubes. The nanotube diameters and wall thickness distributions were evaluated using Nano Measurer software and over 100 measurements were performed.

The functional group composition of the nanomaterials was analyzed by Fourier transform infrared spectroscopy (FTIR, Thermo IS5, USA) over a scanning range of 4000-400 cm^{-1}. Attenuated total reflectance-Fourier transform infrared spectroscopy

(ATR-FTIR, USA) spectra of all membranes, before and after modification, were recorded using a Thermo Nicolet IS10 spectrometer.

X-ray diffraction (XRD, Ultima IV, Japan) analysis was performed to investigate the crystal form of the nanomaterials and membranes, using Cu-Kα radiation (with the following parameters: $\lambda = 0.15418$ nm, tube voltage = 40 kV, tube current = 40 mA, scanning speed = 4 ° min^{-1}).

Nitrogen adsorption isotherms of the MOFs necklaces were measured with an Ankersmid BelSorp max gas sorption analyzer (Netherlands). Before testing, samples were treated at 120 °C in a nitrogen atmosphere for 6 h. The specific surface area values of the nanomaterials were calculated using the multi-point Brunauer-Emmett-Teller (BET) method based on the nitrogen adsorption data.

Thermogravimetric Analysis (TGA, Japan) measurement was conducted using a SHIMADZU TGA-60 instrument, from 25 °C to 900 °C with a heating rate of 5 $°\mathrm{C}\cdot\mathrm{min}^{-1}$ and an N_2 flow rate of 100 $\mathrm{mL}\cdot\mathrm{min}^{-1}$. The proportion of PPy nanotubes in the necklaces was determined by calculating the mass difference between the initial sample and the remaining ash.

Water, *n*-butanol, diiodomethane and glycerine contact angle measurements (Data-Physics OCA-15E contact angle analyzer, Germany) were conducted at 25 °C and 50% relative humidity, using the sessile drop method. A 1 μL liquid droplet was formed at the end of the syringe, and the contact angle data was recorded at the initial contact moment. The reported contact angle values and standard deviations were based on at least five measurements. Time-dependent changes of the *n*-butanol contact angle were recorded until a stable value was obtained, and the real-time contact angle values were measured automatically at regular time intervals.

Simulation models and methods

The ZIF-8 unit cell model was obtained from the Cambridge Crystallographic Data Centre (CCDC, deposition numbers 602542). Crystal growth calculations show that the [100] and [010] surfaces in ZIF-8 dominated the crystalline structure.[1] The ZIF-8 surface model was constructed, considering three-dimensional periodic boundary conditions (3D-PBC), using the Materials Studio software. The models were 54.3 Å in length along the z-direction (three-times the cell size) and 50.9 Å in length along the x and y-direction. The mass transfer channel, with a window-size of 3.4 Å and a cavity size of 11.6 Å, is illustrated in Figure S11;[2] this image was generated using VMD 1.9.3[3] and HOLE[4] software. Figure S12 shows the monomer structure of the PDMS and PPy, and the Packmol[5] program was used to randomly distribute 500 PDMS monomers and 400 PPy monomers in a 45 × 45 × 45 Å box. Subsequently, the Polymatic[6] program was used to bond the initial and terminal points, to obtain 3D-PBC cross-linked PDMS and PPy models.

Jiang *et al.* employed a 7-step compression and relaxation scheme to create a thin membrane, considering two-dimensional periodic boundary conditions (2D-PBC).[7] The scheme consisted of the following 7-steps:

(1) 1×10^4 energy minimization steps were performed to eliminate overlap between atoms. (2) Two 2 nm vacuum layers were initially added on both sides of the PDMS and PPy models along the z axis; then, two impenetrable walls replaced the boundary of the box in the z direction. Subsequently, 300 ps NPT molecular dynamics (MD) simulations at 300 K and 1000 bar compressed a 3D-PBC membrane into a 2D-PBC membrane. (3) 100 ps NVT MD simulations were conducted at 500 K. (4) 100 ps NVT MD simulations were conducted at 300 K. (5) 300 ps NPT MD simulations were conducted at 300 K and 100 bar. (6) Steps (3)–(5) were repeated 20 times until the density difference between two cycles was less than 1 $\mathrm{kg\cdot m^{-3}}$. (7) 1×10^4 ps NPT MD simulations were conducted at 300 K and 1 bar.

The final box size of the PDMS and PPy are 31.68 × 31.68 × 60 Å and 34.85 × 34.85 × 40 Å, respectively. A 5 nm vacuum layer was imposed on both sides of the PDMS box, and 20 butanol molecules and 4029 water molecules were added to construct a 0.5 mol% butanol/water-PDMS system, as shown in Figure S13a. The two PPy boxes were spliced in the middle with a 6 nm thick vacuum layer, and 134 water molecules and 53 butanol molecules were added to the vacuum area, according to the dissolution results for the 0.5 mol% butanol/water-PDMS system. The structure of the 28 mol%

butanol/water-PPy nanotube wall system is shown in Figure S13b. 454 water molecules and 199 butanol molecules were added to both sides of the ZIF-8 surface model to construct the butanol/water-ZIF-8 system, and the initial structure is shown in Figure S13c. As shown in Figure S13d–e, a 5 nm vacuum layer was imposed on both sides of the PPy box and 4054 water molecules and 668 butanol molecules were added to construct the water-PPy system and butanol-PPy system, respectively.

A butanol/water-PDMS system was used to study the dissolution behavior of butanol and water in PDMS. In addition, water-PPy and butanol-PPy systems were used to study the swelling behavior of PPy in these solvents. To eliminate the trade-off between the MD duration and the computational resources, the scheme proposed by Jiang *et al.* was used to accelerate the dissolution behavior of small organic molecules in polymers and the swelling behavior of PPy in solution.[8] The scheme consisted of the following steps:

(1) 1×10^4 energy minimization steps were performed to eliminate overlap between atoms, (2) 500 ps NVT MD simulations were conducted while the temperature was gradually increased from 300 to 500 K, (3) 500 ps NVT MD simulations were conducted at 500 K, (4) 500 ps NVT MD simulations were conducted while the temperature was gradually decreased from 500 to 300 K, (5) 1500 ps NVT MD simulations were conducted at 300 K, and (6) 1000 ps NP_zT MD simulations were conducted at 300 K and 1 bar, with the pressure along the z-axis maintained at 1 bar to allow the size of the simulation box to vary along the z-axis, while the size of the simulation box was fixed in x- and y-axis directions. (7) Steps (2)–(6) were repeated 14 times until the density difference between two cycles was less than 1 $kg\cdot m^{-3}$. (8) 1×10^4 ps NP_zT MD simulations were performed at 300 K and 1 bar.

The butanol/water-PPy nanotube wall system was used to study the distribution of butanol and water on the PPy wall. First, 1×10^4 energy minimization steps were performed to eliminate overlap between atoms, and then the NVT MD simulation was performed at 300 K for 2 ns. A butanol/water-ZIF-8 system was used to study the adsorption behavior of water and butanol on ZIF-8, and the same MD method was used as described above for the butanol/water-PPy nanotube wall system. Furthermore, a single guest molecule (water or butanol) was placed in close proximity to the ZIF-8 and PDMS to compare the diffusion rate of guest molecules through PDMS and ZIF-8. This guest molecule was allowed to accelerate at 2 nm.ps^{-2} along the z-axis direction to enable it to pass through the ZIF-8 and PDMS.

The MD simulations were performed using the GROMACS v5.0.6[9] package. PPy and butanol were described by the OPLS[10] force field. Water was described by the three-point potential (TIP3P) model,[11] while the force field parameter of PDMS was taken from Sok *et al.*[12] and the force field parameter of ZIF-8 was taken from Marco Sant *et al.*[13] The non-bond interactions were described by the Lennard-Jones (LJ) and the Ewald methods. The LJ interactions were truncated at 1.4 nm in conjunction with a switching function. The combinatory rules of the LJ parameters were described by Lorentz-Berthelot. The equations of motion were integrated using a leap-frog algorithm and the time step was 1 fs. The temperature was maintained by a Nosé-Hoover thermostat and the initial velocity was generated using a Gaussian distribution at 300 K. The pressure was controlled by the Berendsen barostat in a semi-isotropic manner to reach equilibrium and then by the Parrinello-Rahman barostat in a semi-isotropic manner. The force field parameters of the PDMS and PPy are shown in Tables S3-S7.

Figures

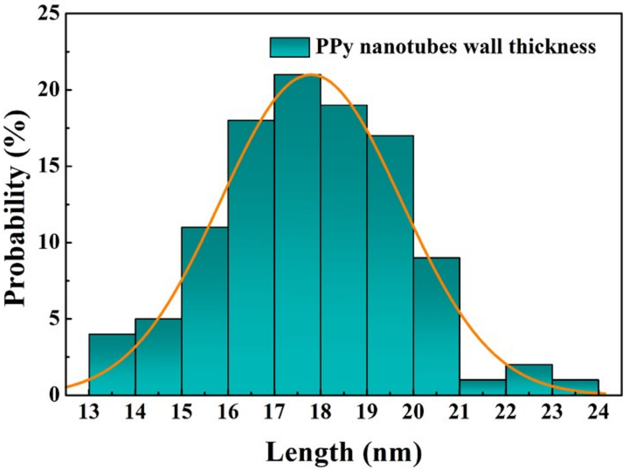

Fig. S1 Wall thickness distribution histogram for the PPy nanotubes.

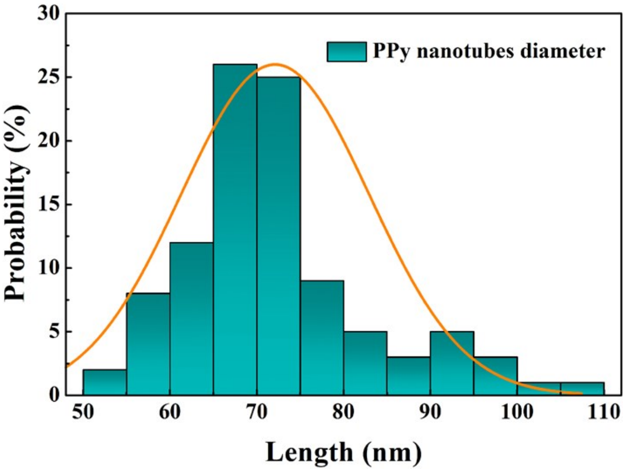

Fig. S2 Diameter distribution histogram for the PPy nanotubes.

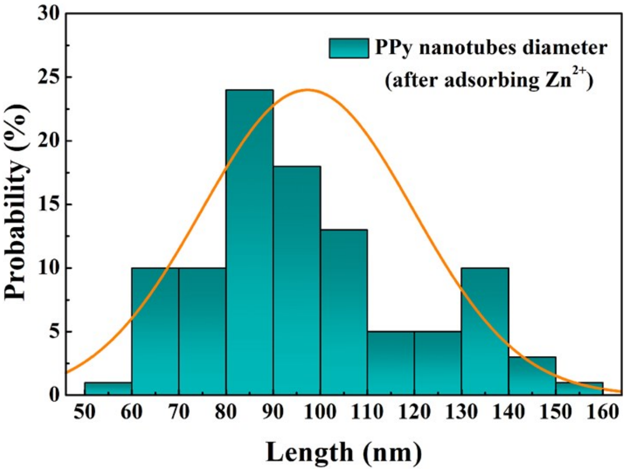

Fig. S3 Diameter distribution histogram for the PPy nanotubes after adsorption of Zn^{2+} ions.

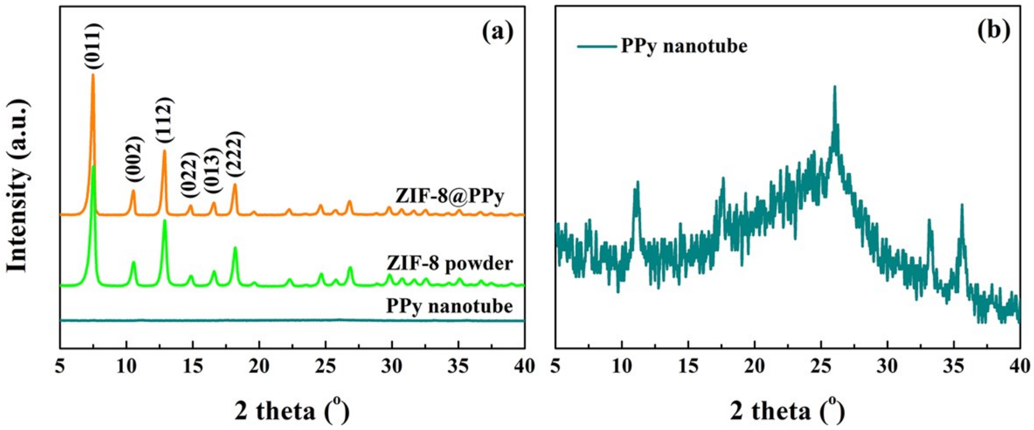

Fig. S4 XRD patterns of the ZIF-8@PPy pearl necklace. (a) ZIF-8@PPy pearl necklace and (b) PPy nanotube.

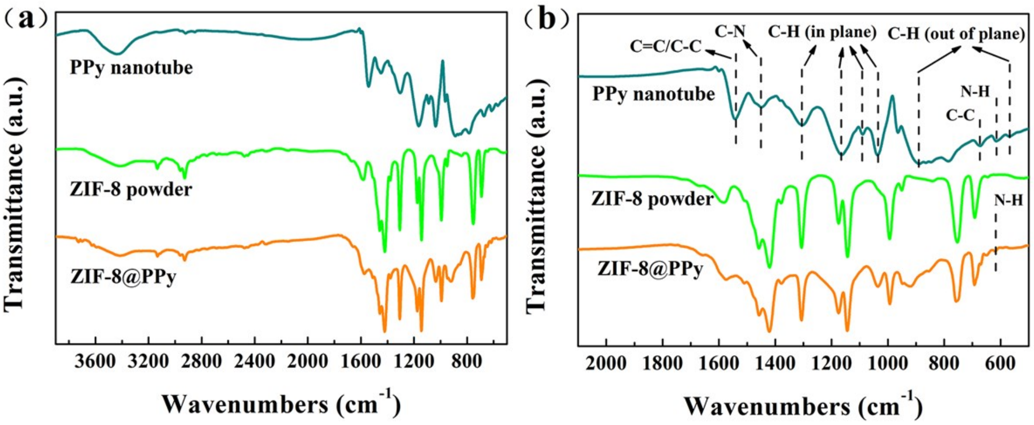

Fig. S5 FTIR spectra of the ZIF-8@PPy pearl necklace.

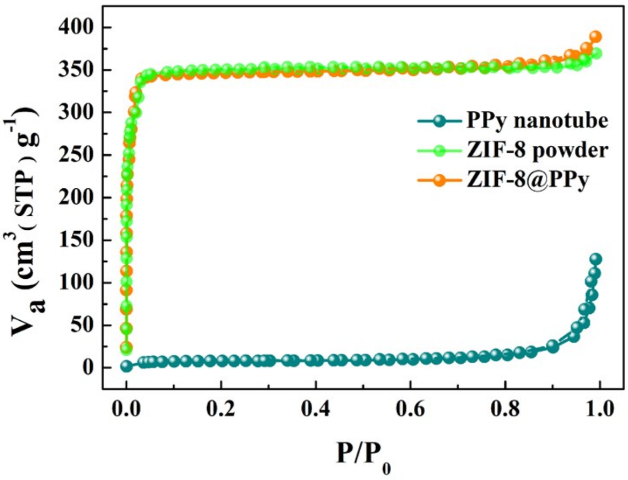

Fig. S6 N_2 adsorption/desorption isotherms for the ZIF-8@PPy pearl necklace.

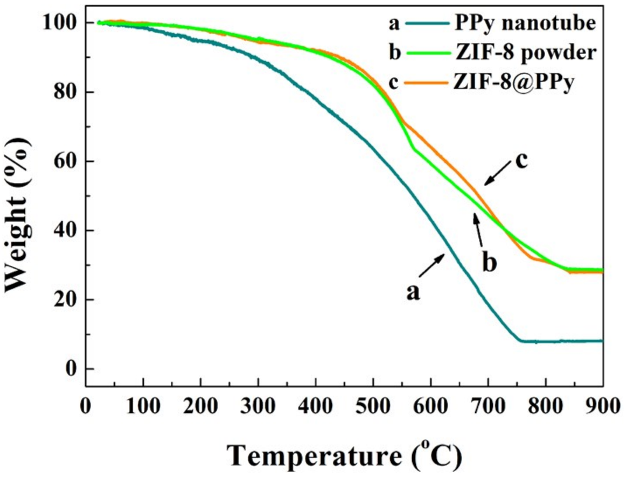

Fig. S7 TGA of the ZIF-8@PPy pearl necklace.

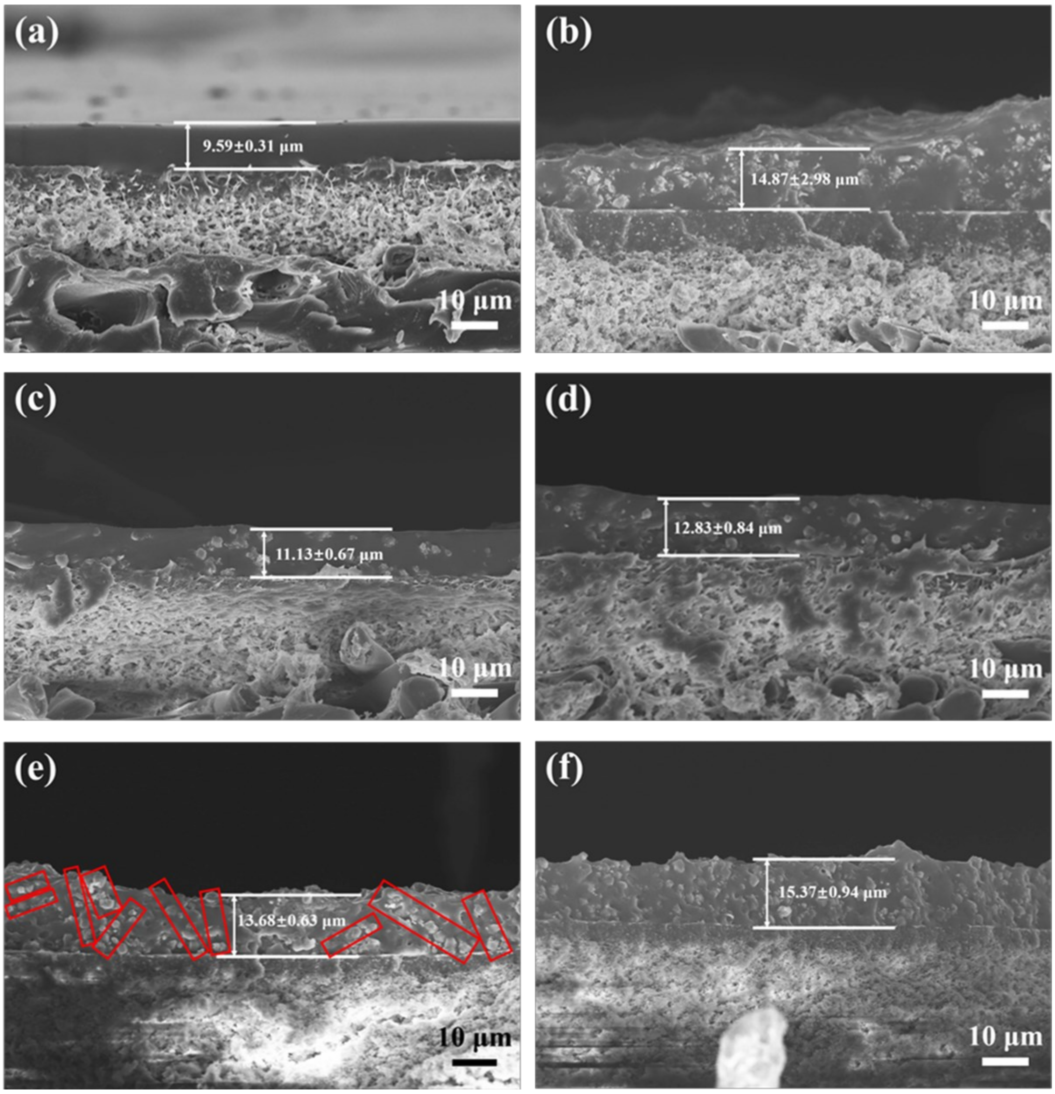

Fig. S8 Cross sectional SEM images of ZIF-8@PPy-X/PDMS. (a) Pristine PDMS. (b) PPy/PDMS. (c) ZIF-8@PPy5/PDMS. (d) ZIF-8@PPy10/PDMS. (e) ZIF-8@PPy20/PDMS, and (f) ZIF-8@PPy30/PDMS membranes.

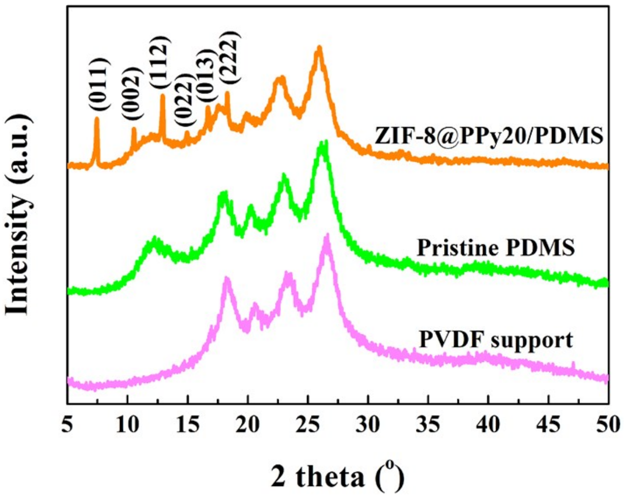

Fig. S9 XRD patterns of the ZIF-8@PPy20/PDMS membranes.

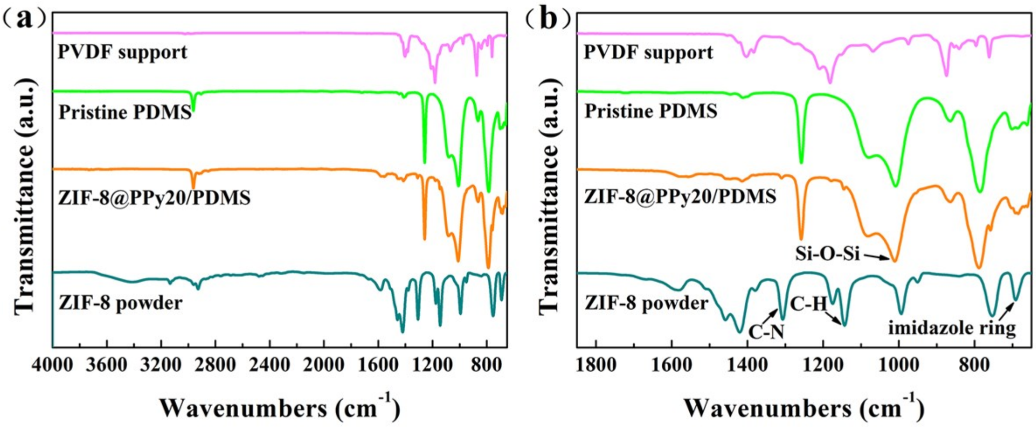

Fig. S10 FTIR spectra of the ZIF-8@PPy20/PDMS membranes.

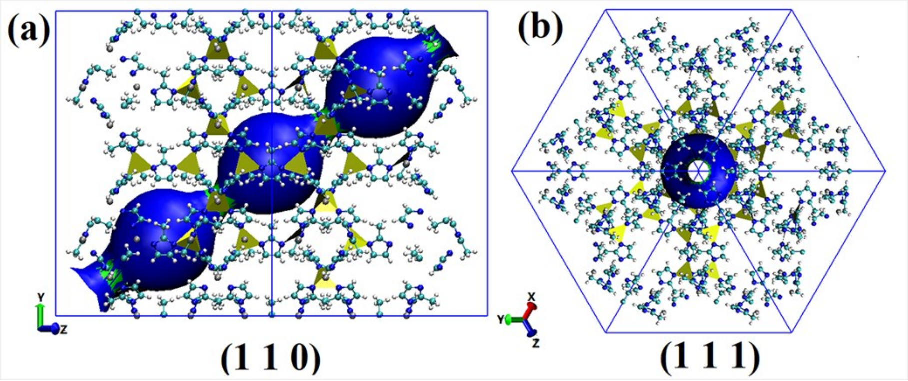

Fig. S11 Channel structure of ZIF-8. (a) and (b) from different perspectives. Color label: Zn (yellow polyhedron), C (cyan), H (white), channel (blue), window (green).

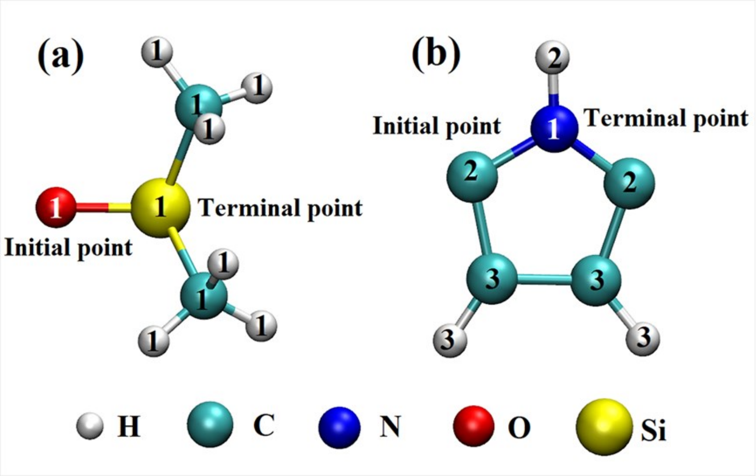

Fig. S12 Monomer structures of PDMS and PPy. (a) PDMS. (b) PPy. Color label: H (white), C (cyan), N (blue), O (red), Si (yellow).

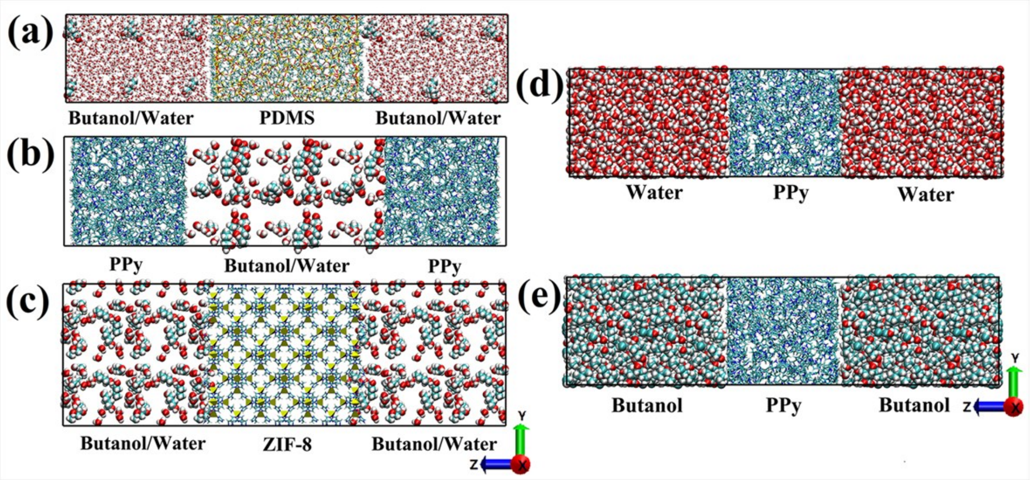

Fig. S13 Initial structure of the butanol/water-PDMS, butanol/water-PPy nanotube wall, butanol/water-ZIF-8, water-PPy, and butanol-PPy systems. (a) Butanol/water-PDMS system. (b) Butanol/water-PPy nanotube wall system. (c) Butanol/water-ZIF-8 system. (d) Water-PPy system. (e) Butanol-PPy system.

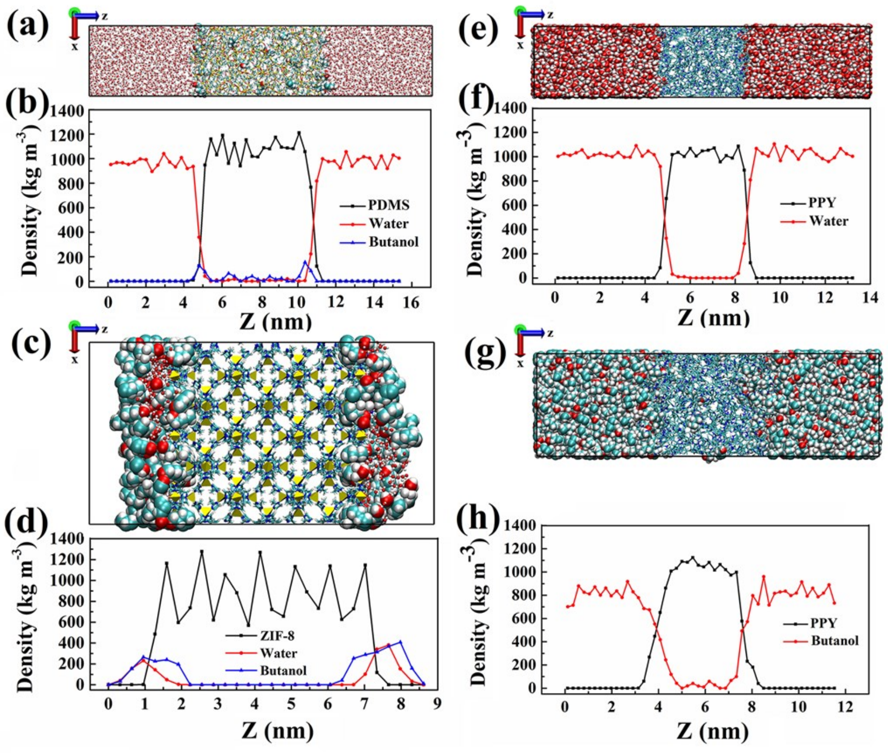

Fig. S14 Solution form of the butanol/water or one component system on PDMS, ZIF-8, PPy and PPy nanotube wall. (a) The final structure of the butanol/water-PDMS system. (b) The density profile of the butanol/water-PDMS system along the z-direction. (c) The final structure of the butanol/water-ZIF-8 system. Blue ball (butanol), purple ball (water). (d) The density profile of the butanol/water-ZIF-8 system along the z-direction. (e) The final structure of water-PPy system. (f) The density profile of the water-PPy system along the z-direction. (g) The final structure of butanol-PPy system. (h) The density profile of the butanol-PPy system along the z-direction.

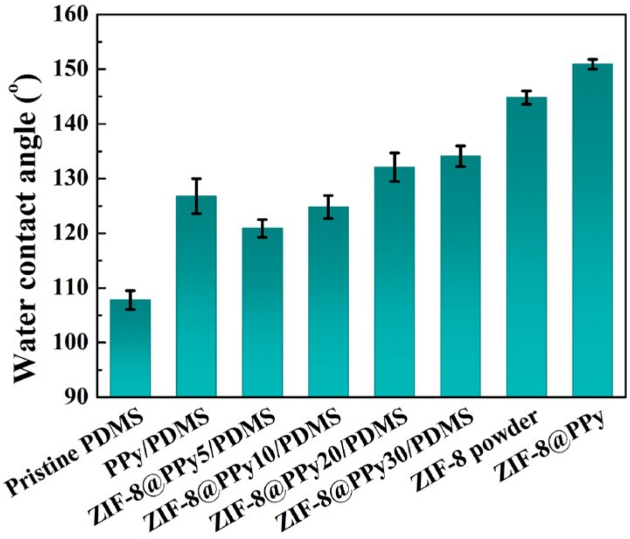

Fig. S15 Water contact angle of ZIF-8@PPy pearl necklace powder and ZIF-8@PPy-x/PDMS.

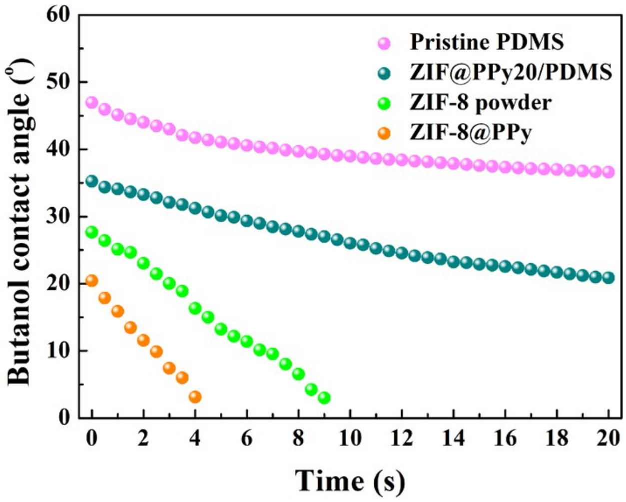

Fig. S16 Butanol contact angle of ZIF-8@PPy pearl necklace powder and ZIF-8@PPy20/PDMS with increasing time.

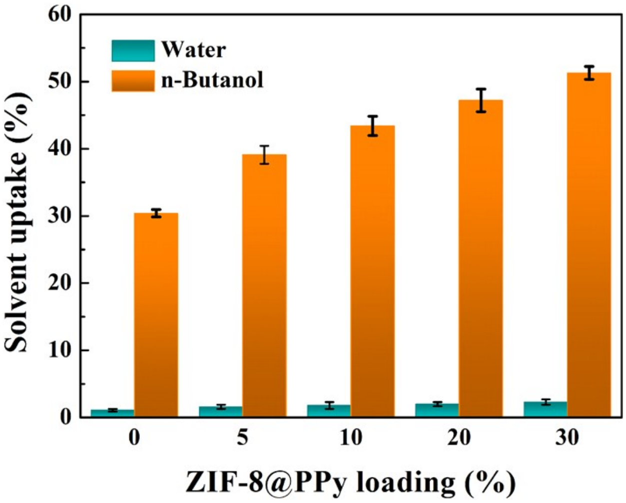

Fig. S17 Solvent uptake of the membranes with different ZIF-8@PPy loading.

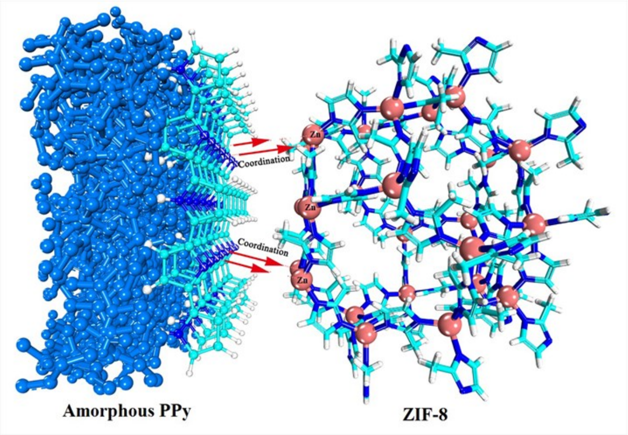

Fig. S18 Interface enlargement of the ZIF-8@PPy pearl necklace: “Small World”.

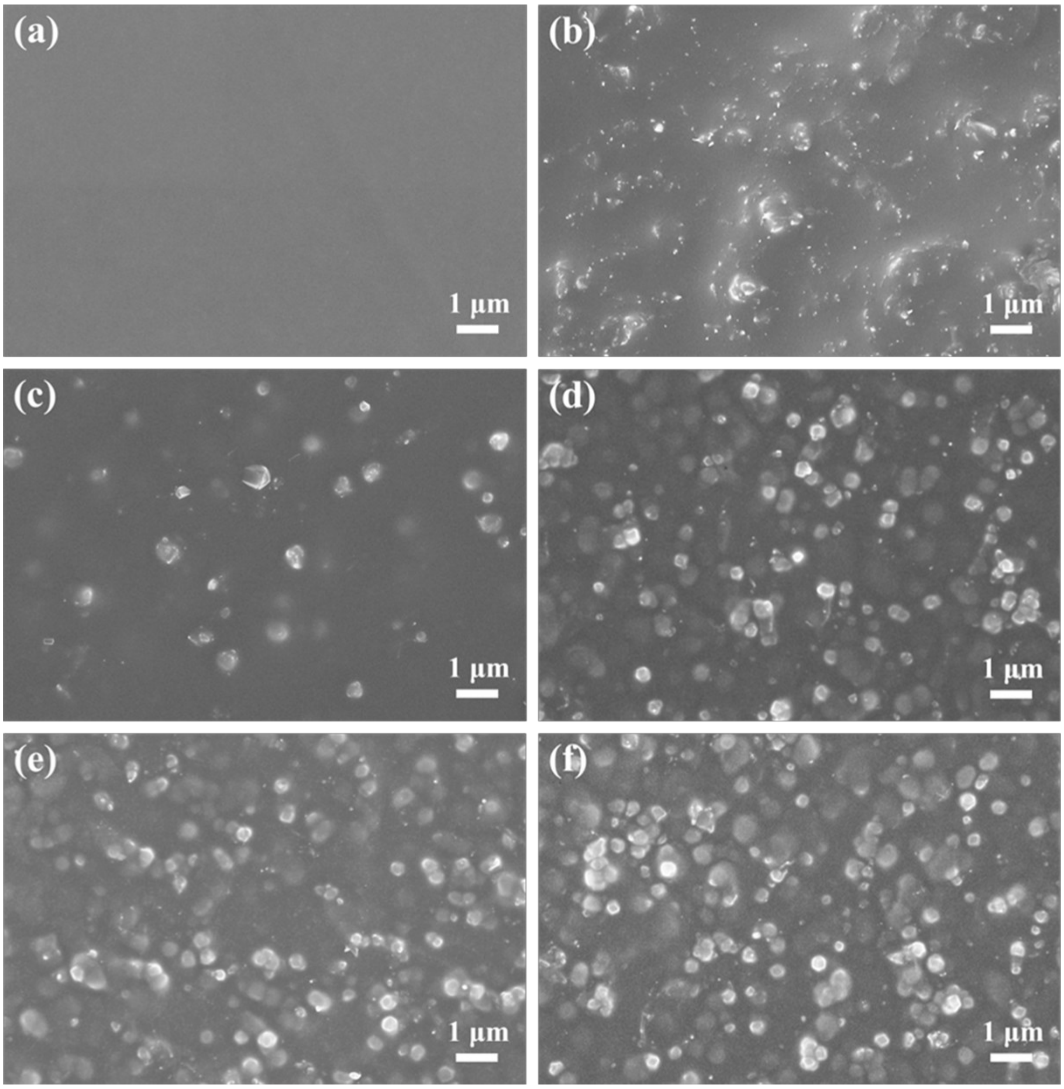

Fig. S19 SEM images of the ZIF-8@PPy-X/PDMS membranes surfaces. (a) Pristine PDMS. (b) PPy/PDMS. (c) ZIF-8@PPy5/PDMS. (d) ZIF-8@PPy10/PDMS. (e) ZIF-8@PPy20/PDMS. (f) ZIF-8@PPy30/PDMS membranes.

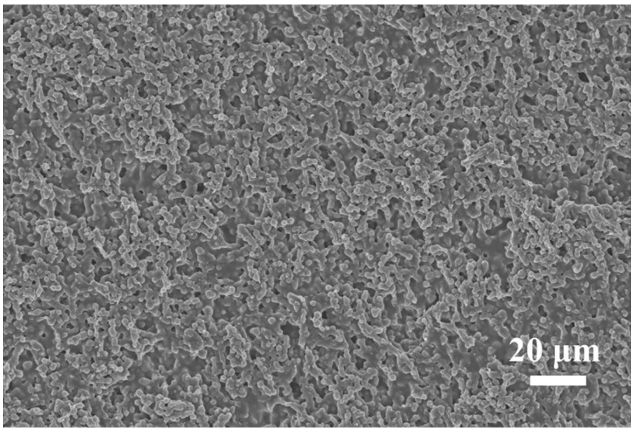

Fig. S20 SEM images of the ZIF-8@PPy60/PDMS membrane surfaces.

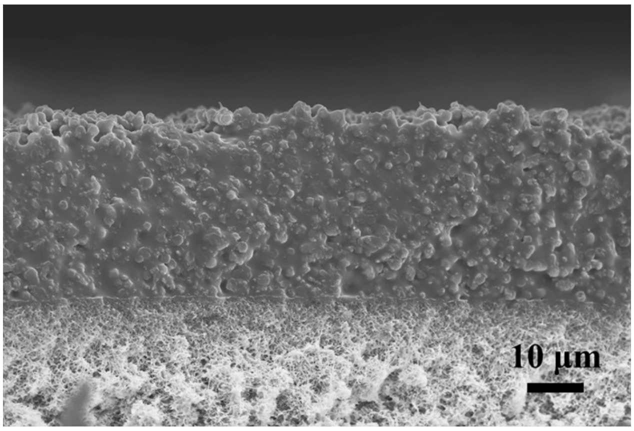

Fig. S21 SEM images of the ZIF-8@PPy60/PDMS membrane cross-section.

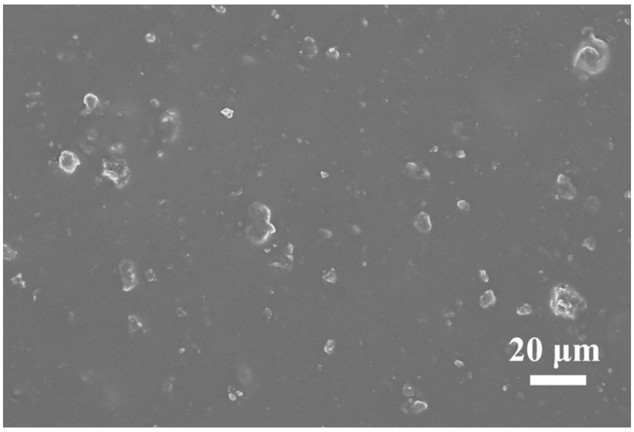

Fig. S22 SEM images of the ZIF-8/PDMS membrane surfaces. The ZIF-8/PDMS membranes were prepared by embedding 20 wt% isolated ZIF-8 particles without PPy nanotube in PDMS.

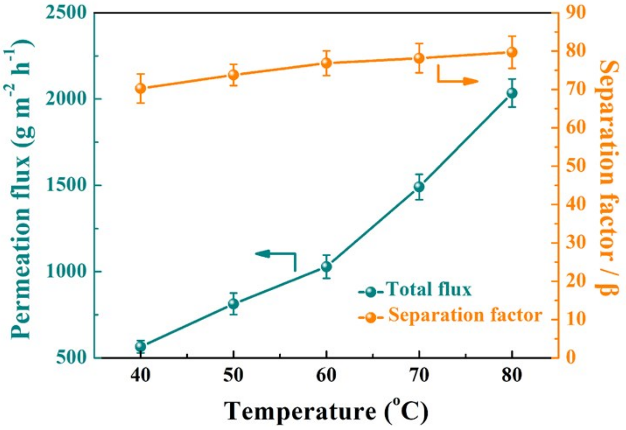

Fig. S23 Effect of the feed temperature on the pervaporation performance of ZIF-8@PPy20/PDMS for separating 1 wt% *n*-butanol aqueous solutions.

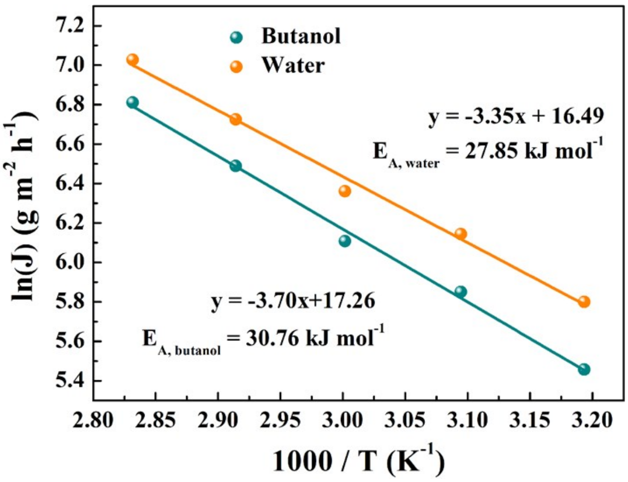

Fig. S24 Arrhenius plots of *n*-butanol and water fluxes of the ZIF-8@PPy20/PDMS membranes for separating 1 wt% *n*-butanol aqueous solution.

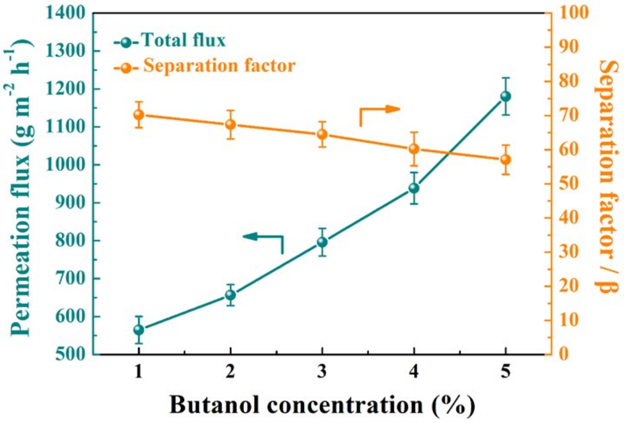

Fig. S25 Effect of *n*-butanol concentration on the pervaporation performance of ZIF-8@PPy20/PDMS at 40 °C with a flow of 80 L.h^{-1}.

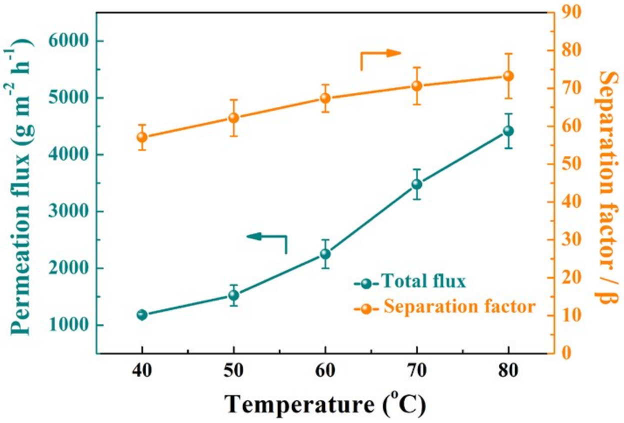

Fig. S26 Effect of the feed temperature on the pervaporation performance of ZIF-8@PPy20/PDMS with a flow of 80 L.h^{-1} for separating 5 wt% *n*-butanol aqueous solutions.

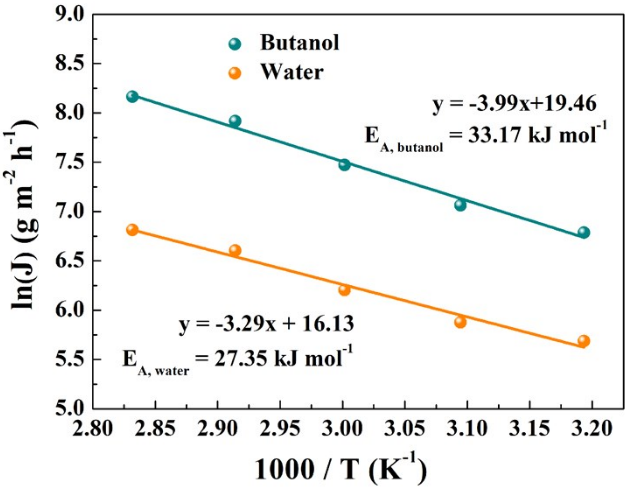

Fig. S27 Arrhenius plots of *n*-butanol and water fluxes of ZIF-8@PPy20/PDMS membranes for separating 5 wt% *n*-butanol aqueous solution.

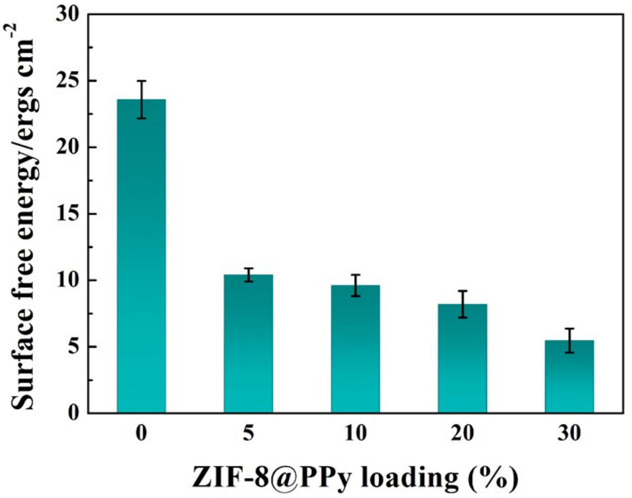

Fig. S28 Surface free energy of membranes with different ZIF@PPy loading.

Tables

Table S1. Comparison of the pervaporation performance of various membranes in separating 1 wt% *n*-butanol aqueous solution at 40 °C.

Membrane	Loading amount (wt%)	Active layer Thickness (μm)	Total flux (g.m^{-2}.h^{-1})	Separation factor	Ref.
Silicalite-1/PDMS	20	3	750	17	(2019) [14]
ZIF-7/PDMS	20	20	760	47	(2016) [15]
PEBA/hollow fiber	---	2	2000	20	(2016) [16]
ZIF-L/PDMS	30	17.3	402	57.6	(2019) [17]
POSS/PDMS	40	9	745	40	(2015) [18]
PDMS/ceramic	---	---	820	32	(2015) [19]
Zn(BDC)(TED)$_{0.5}$/PEBA	10	---	700	16.5	(2014) [20]
	20	---	590	18.3	
CNTs/PDMS	10	---	60	24	(2014) [21]
ILs/PVDF	---	29	390	36.2	(2013) [22]
ZIF-71/PEBA	20	15	575	20	(2013) [23]
	25	15	400	22.3	
PERVAP-1060	---	190	340	18.9	(1997) [24]
PERVAP-1070	---	210	90	36	
ZHNTs/PDMS	15	12.2	683	61.3	(2020) [25]
PDMS/hollow fiber	---	10	1282	42.9	(2014) [26]
PDMS/PVDF	---	11	770	42	(2019) [27]
PIM-1/PDMS	8	22	600	25	(2019) [28]
CHNs/PDMS	---	0.21	3150	30	(2019) [29]
PDecMS/MFFK-1	---	4.5	170	61.5	(2020) [30]
CMX-GF-010-D	---	10	330	39	(2009) [31]
PERTHESE 500-1	---	125	33	56	(2009) [31]
HPSiO-c-PDMS	---	20	520	39.3	(2015) [32]
ZIF-8@PPy/PDMS	20	13.68	564.8	70.2	This work
ZIF-8@PPy/PDMS	30	15.37	478.1	75.0	This work

Table S2. Comparison of butanol/water separation pervaporation performance between various membranes under other conditions. The best permeation separation performance values were selected, and membranes with thickness less than 100 μm were chosen based on considering the required permeability in possible industrial applications. The butanol permeability and selectivity are calculated by equations 9-11.

Membrane type	Feed conc. (wt %)	Feed temp. (°C)	Butanol Permeability / 1000 barrer	Selectivity / α	sign	Ref.
PPhS/PDMS/PVDF	1	30	61.47	3.19	■	(2014) [33]
PERVAP-2200	1	33	3.66	0.67	■	(2006) [34]
PDMS/PE/Brass	1	37	74.80	2.21	■	(2010) [35]
PDMS/PAN	1	42	35.58	1.39	■	(2013) [36]
Slicate-1/PDMS	1	50	70.90	3.62	■	(2011) [37]
PDMS/PEI	1	60	1.15	4.29	■	(2014) [38]
ZIF-8–PDMS	1	80	9.22	4.45	●	(2014) [39]
CZIF-8/PDMS	1.2	55	63.66	1.20	●	(2019) [40]
PTMSP-SNPs	1.5	50	55.64	5.19	▲	(2020) [41]
PDMSc	1.5	55	94.59	2.67	▲	(2013) [42]
O-ZIF-8@PDA/PDMS	1.5	55	73.13	3.42	●	(2019) [43]
CZIF-8/PDMS	1.5	55	78.89	3.24	●	(2019) [44]
ZIF-8/PDMS	1.5	55	151.22	2.59	●	(2020) [45]
MA-PDMS	1.5	55	105.84	2.88	▲	(2019) [46]
Silicalite-1/MA-PDMS	1.5	55	119.29	4.28	▲	(2019) [46]
PTMSP	1.5	70	66.08	4.06	▲	(2001) [47]
VA-CNT/PDMS	1.5	80	100.83	2.11	▲	(2019) [48]
$P_{6,6,6,14}[TF_2N]$/PDMS	2	30	46.41	3.31	⬟	(2019) [49]
MCM-41–PEBA	2.5	35	139.97	1.86	⬟	(2014) [50]
IL-GO-PEBA	2.5	35	130.10	1.99	⬟	(2019) [51]
MCM-41-IL-PEBA	2.5	35	111.26	1.89	⬟	(2019) [52]
MFI	3	60	2.12	0.66	⬟	(2013) [53]
COF-LZU1/PDMS	3.6	64	119.00	2.65	●	(2020) [54]
COF-LZU1/PEBA	3.7	34	169.65	1.79	●	(2019) [55]
CTF/PDMS	4	60	56.37	4.44	●	(2020) [56]
PEBA	5	23	58.00	0.67	●	(2005) [57]
PhTMS	5	30	232.04	2.44	●	(2012) [58]
CB–PIM-1	5	30	213.86	1.78	●	(2019) [59]
PEBA-IL	5	37	18.79	2.01	●	(2012) [60]
PDMS-PhTMS	5	40	88.96	4.29	●	(2020) [61]
ZIF-7-NH_2/Pebax	5	40	58.06	1.58	◆	(2020) [62]
ZIF-8GO/PEBA	5	55	2.63	2.26	●	(2020) [63]
PDMS ^{CF3}	5	60	2.55	2.06	◆	(2013) [64]
ZIF-8/PDMS	5	80	4.86	3.71	●	(2014) [65]
COF-300/PDMS	5	80	81.35	2.78	◆	(2019) [66]
COF-42	5	80	11.22	8.40	◆	(2018) [67]
PVDF	7.5	50	61.52	0.60	◆	(2007) [68]
ZIF-8@PPy30/PDMS	1	40	125.24	4.80	★	This work
ZIF-8@PPy20/PDMS	5	80	64.50	5.30	★	This work

Table S3. Nonbond parameter and charge distribution.

$$E_{\text{nonbond}}(r) = 4\varepsilon((\frac{\sigma}{r})^{12} - (\frac{\sigma}{r})^{6})$$

Element Type	Force-field Type	q (e)	σ (nm)	ε (kJ.mol^{-1})
PDMS				
C1	CT	-0.294	0.3500	0.2761
O1	OS	-0.445	0.2900	0.8439
H1	HC	0.053	0.2500	0.1255
Si1	SI	0.715	0.3385	2.4470
PPy				
N1	NA	-0.727	0.3250	0.7113
C2	CW	0.187	0.3550	0.2929
C3	CT	-0.053	0.3500	0.2761
H2	HA	0.353	0.2510	0.0628
H3	HC	0.053	0.2470	0.0657

Table S4. Bond parameters.

$$E_{\text{bond}}(r) = \frac{1}{2}k_{\text{b}}(r - r_0)$$

Bond	r_0 (nm)	k_{b} (kJ.mol^{-1}.nm^{-2})
PDMS		
CT-HC	0.10900	284512.0
SI-OS	0.16300	251040.0
SI-CT	0.18800	200000.0
PPy		
HA-NA	0.10100	363171.2
NA-CW	0.13810	357314.0
CW-CT	0.15040	265265.6
CT-HC	0.10900	284512.0
CT-CT	0.15260	259408.0
CW-CW	0.13430	345000.0

Table S5. Angle parameters.

$$E_{\mathrm{angle}}(\theta) = \frac{1}{2} k_{\mathrm{a}}(\theta - \theta_0)$$

Angle	θ_0 (deg)	k_{a} (kJ.mol^{-1}.rad^{-2})
PDMS		
HC-CT-SI	110.700	313.800
OS-SI-CT	109.500	418.400
SI-OS-SI	144.400	118.400
OS-SI-OS	109.500	791.200
CT-SI-CT	109.500	418.400
PPy		
HA-NA-CW	120.000	292.880
NA-CW-CT	110.000	585.760
NA-CW-CW	107.100	1004.000
CW-CT-HC	120.500	292.880
CW-CT-CT	106.000	527.184
CW-CW-CT	120.000	585.760

Table S6. Proper dihedral angle parameters.

$$E_{\mathrm{dihedral\ angle}}(\phi) = k_{\phi}(1 + \cos(n\phi - \phi_{\mathrm{s}}))$$

Dihedral	k_{Φ} (kJ.mol^{-1})	Φ_{s} (deg)	n
PDMS			
HC-CT-SI-OS	0.0000	0.0	0
HC-CT-SI-CT	0.0000	0.0	0
CT-SI-OS-SI	3.7700	0.0	3
OS-SI-OS-SI	3.7700	0.0	3
SI-OS-SI-OS	3.7700	0.0	3
PPy			
HA-NA-CW-CT	21.2570	180.0	2
HA-NA-CW-CW	0.0000	0.0	0
NA-CW-CT-CT	21.2570	180.0	2
NA-CW-CW-NA	0.0000	0.0	0
NA-CW-CW-CT	0.0000	0.0	0
CW-CT-CT-CW	21.2570	180.0	2
CW-CW-CT-HC	0.0000	0.0	0
CW-CW-CT-CT	0.0000	0.0	0
CW-CT-CT-HC	21.2570	180.0	2
HC-CT-CT-HC	0.6280	0.0	3

Table S7. Improper dihedral angle parametexdrs.

$$E_{\text{improper dihedral}}(\phi) = k_{\phi}(1 + \cos(n\phi - \phi_s))$$

Dihedral	k_{Φ} (kJ.mol^{-1}.rad^{-2})	Φ_s (deg)	n
PPy			
CW-CW-CT-NA	0.0000	0.0	0
CW-CT-CT-HC	4.6024	180.0	2
CW-NA-CW-HA	4.1840	180.0	2

Table S8. Free volume parameters of pristine PDMS, PPy/PDMS, ZIF-8/PDMS and ZIF-8@PPy20/PDMS membranes.

Membranes	$\tau_{3\text{-}1}$/ns	$\tau_{3\text{-}2}$/ns	$R_{3\text{-}1}$/Å	$R_{3\text{-}2}$/Å	$V_{\text{F},3\text{-}1}$/Å^3	$V_{\text{F},3\text{-}2}$/Å^3
Pristine PDMS-fs	1.12	3.49	1.84	3.94	26.09	256.20
PPy/PDMS-fs	1.35	3.49	2.15	3.94	41.63	256.20
ZIF-8/PDMS-fs	0.69	3.51	1.02	3.96	13.76	260.10
ZIF-8@PPy20/PDMS-fs	1.88	3.65	2.74	4.04	86.17	276.21

References

1. R. Semino, N. A. Ramsahye, A. Ghoufi and G. Maurin, *ACS Appl. Mater. Inter.*, 2016, **8**, 809-819.
2. X. C. Huang, Y. Y. Lin, J. P. Zhang and X. M. Chen, *Angew. Chem. Int. Edit.*, 2006, **45**, 1557-1559.
3. W. Humphrey, A. Dalke and K. Schulten, *J. Mol. Graph.*, 1996, **14**, 33-38.
4. O. S. Smart, J. M. Goodfellow and B. A. Wallace, *Biophys. J.*, 1993, **65**, 2455-2460.
5. L. Martinez, R. Andrade, E. G. Birgin and J. M. Martinez, *J. Comput. Chem.*, 2009, **30**, 2157-2164.
6. L. J. Abbott, K. E. Hart and C. M. Colina, *Theor. Chem. Acc.*, 2013, **132**, 1334.
7. Q. Shi, K. Zhang, R. Lu and J. Jiang, *J. Membr. Sci.*, 2018, **545**, 49-56.
8. J. Liu, Q. Xu and J. Jiang, *J. Membr. Sci.*, 2019, **573**, 639-646.
9. D. Van Der Spoel, E. Lindahl, B. Hess, G. Groenhof, A. E. Mark and H. J. C. Berendsen, *J. Comput. Chem.*, 2005, **26**, 1701-1718.
10. W. L. Jorgensen, D. S. Maxwell and J. Tirado-Rives, *J. Am. Chem. Soc.*, 1996, **118**, 11225-11237.
11. W. L. Jorgensen, J. Chandrasekhar, J. D. Madura, R. W. Impey and M. L. Klein, *J. Chem. Phys.*, 1983, **79**, 926-935.
12. R. M. Sok, H. J. C. Berendsen and W. F. V. Gunsteren, *J. Chem. Phys.*, 1992, **96**, 4699-4704.
13. B. Zheng, M. Sant, P. Demontis and G. B. Suffritti, *J. Phys. Chem. C*, 2012, **116**, 933-938.
14. J. Y. Lee, S. O. Hwang, H. -J. Kim, D. -Y. Hong, J. S. Lee and J. -H. Lee, *Sep. Purif. Technol.*, 2019, **209**, 383-391.
15. X. Wang, J. Chen, M. Fang, T. Wang, L. Yu and J. Li, *Sep. Purif. Technol.*, 2016, **163**, 39-47.
16. Y. Li, J. Shen, K. Guan, G. Liu, H. Zhou and W. Jin, *J. Membr. Sci.*, 2016, **510**, 338-347.

17. H. Mao, H. -G. Zhen, A. Ahmad, S. -H. Li, Y. Liang, J. -F. Ding, Y. Wu, L. -Z. Li and Z. -P. Zhao, *J. Membr. Sci.*, 2019, **582**, 307-321.
18. G. Liu, W. -S. Hung, J. Shen, Q. Li, Y. -H. Huang, W. Jin, K. -R. Lee and J. -Y. Lai, *J. Mater. Chem. A*, 2015, **3**, 4510-4521.
19. D. Liu, G. Liu, L. Meng, Z. Dong, K. Huang and W. Jin, *Sep. Purif. Technol.*, 2015, **146**, 24-32.
20. S. Liu, G. Liu, J. Shen and W. Jin, *Sep. Purif. Technol.*, 2014, **133**, 40-47.
21. C. Xue, G. -Q. Du, L. -J. Chen, J. -G. Ren, J. -X. Sun, F. -W. Bai and S. -T. Yang, *Sci. Rep.*, 2014, **4**, 5925.
22. H. Cascon and S. Choudhary, *Sep. Sci. Technol.*, 2013, **48**, 1616-1626.
23. S. Liu, G. Liu, X. Zhao and W. Jin, *J. Membr. Sci.*, 2013, **446**, 181-188.
24. A. Jonquieres and A. Fane, *J. Membr. Sci.*, 1997, **125**, 245-255.
25. H. Mao, S. -H. Li, A. -S. Zhang, L. -H. Xu, J. -J. Lu and Z. -P. Zhao, *J. Membr. Sci.*, 2020, **595**, 117543.
26. Z. Dong, G. Liu, S. Liu, Z. Liu and W. Jin, *J. Membr. Sci.*, 2014, **450**, 38-47.
27. Y. Pan, Y. Hang, X. Zhao, G. Liu and W. Jin, *J. Membr. Sci.*, 2019, **579**, 210-218.

28. G. Zhang, H. Cheng, P. Su, X. Zhang, J. Zheng, Y. Lu and Q. Liu, *Sep. Purif. Technol.*, 2019, **216**, 83-91.
29. Y. Ji, G. Chen, G. Liu, J. Zhao, G. Liu, X. Gu and W. Jin, *ACS Appl. Mater. Inter.*, 2019, **11**, 36717-36726.
30. E. A. Grushevenko, I. A. Podtynnikov and I. L. Borisov, *Russ. J. Appl. Chem.*, 2020, **92**, 1593-1601.
31. V. García, E. Pongracz, E. Muurinen and R. L. Keiski, *Desalination*, 2009, **241**, 201-211.
32. Y. Bai, L. Dong, J. Lin, Y. Zhu, C. Zhang, J. Gu, Y. Sun and Y. Xu, *RSC Adv.*, 2015, **5**, 52759-52768.
33. K. Y. Jee and Y. T. Lee, *J. Membr. Sci.*, 2014, **456**, 1-10.
34. E. E-Zanati, E. A-Hakim, O. E-Ardi and M. Fahmy, *J. Membr. Sci.*, 2006, **280**, 278-283.

35. S. -Y. Li, R. Srivastava and R. S. Parnas, *J. Membr. Sci.*, 2010, **363**, 287-294.
36. J. Niemistö, W. Kujawski and R. L. Keiski, *J. Membr. Sci.*, 2013, **434**, 55-64.
37. H. Zhou, Y. Su, X. Chen and Y. Wan, *Sep. Purif. Technol.*, 2011, **79**, 375-384.
38. L. T. P. Trinh, Y. J. Lee, H. -J. Bae and H. -J. Lee, *J. Ind. Eng. Chem.*, 2014, **20**, 2814-2818.
39. H. Fan, Q. Shi, H. Yan, S. Ji, J. Dong and G. Zhang, *Angew. Chem. Int. Edit.*, 2014, **53**, 5578-5582.
40. Z. Si, D. Cai, S. Li, C. Zhang, P. Qin and T. Tan, *J. Membr. Sci.*, 2019, **579**, 309-317.
41. V. P. Talluri, A. Tleuova, S. Hosseini and O. Vopicka, *Membranes*, 2020, **10**, 55.
42. S. Li, F. Qin, P. Qin, M. N. Karim and T. Tan, *Green Chem.*, 2013, **15**, 2180-2190.
43. S. Li, Z. Chen, Y. Yang, Z. Si, P. Li, P. Qin and T. Tan, *Sep. Purif. Technol.*, 2019, **215**, 163-172.
44. Z. Si, D. Cai, S. Li, G. Li, Z. Wang and P. Qin, *Sep. Purif. Technol.*, 2019, **221**, 286-293.
45. G. Li, Z. Si, D. Cai, Z. Wang, P. Qin and T. Tan, *Sep. Purif. Technol.*, 2020, **236**, 116263.
46. Z. Si, J. Li, L. Ma, D. Cai, S. Li, J. Baeyens, J. Degrève, J. Nie, T. Tan and P. Qin, *Angew. Chem. Int. Edit.*, 2019, **58**, 17175-17179.
47. A. G. Fadeev, Y. S. Selinskaya, S. S. Kelley, M. M. Meagher, E. G. Litvinova, V. S. Khotimsky and V. V. Volkov, *J. Membr. Sci.*, 2001, **186**, 205-217.
48. D. Yang, C. Cheng, M. Bao, L. Chen, Y. Bao and C. Xue, *J. Membr. Sci.*, 2019, **577**, 51-59.
49. R. Cabezas, K. Suazo, G. Merlet, E. Quijada-Maldonado, A. Torresb and J. Romero, *RSC Adv.*, 2019, **9**, 8546-8556.
50. H. Tan, Y. Wu, Y. Zhou, Z. Liu and T. Li, *J. Membr. Sci.*, 2014, **453**, 302-311.
51. W. Tang, H. Lou, Y. Li, X. Kong, Y. Wu and X. Gu, *J. Membr. Sci.*, 2019, **581**, 93-104.
52. Y. Li, D. Yan and Y. Wu, *R. Soc. Open Sci.*, 2019, **6**, 190291.

53. D. Korelskiy, T. Leppäjärvi, H. Zhou, M. Grahn, J. Tanskanen and J. Hedlund, *J. Membr. Sci.*, 2013, **427**, 381-389.
54. G. Wu, X. Lu, Y. Li, Z. Jia, X. Cao, B. Wang and P. Zhang, *Sep. Purif. Technol.*, 2020, **241**, 116406.
55. G. Wu, Y. Li, Y. Geng and Z. Jia, *J. Membr. Sci.*, 2019, **581**, 1-8.
56. J. Y. Lee, H. Park, J. S. Lee, S. Yoon and J. -H. Lee, *J. Membr. Sci.*, 2020, **598**, 117654.
57. F. Liu, L. Liu and X. Feng, *Sep. Purif. Technol.*, 2005, **42**, 273-282.
58. E. J. Jeon, A. S. Kim and Y. T. Lee, *Desalin. Water Treat.*, 2012, **48**, 17-26.
59. Y. Lan and P. Peng, *J. Appl. Polym. Sci.*, 2019, **136**, 46912.
60. S. Heitmann, J. Krings, P. Kreis, A. Lennert, W. R. Pitner, A. Górak and M. M. Schulte, *Sep. Purif. Technol.*, 2012, **97**, 108-114.
61. J. Y. Lee, J. S. Lee and J. -H. Lee, *Sep. Purif. Technol.*, 2020, **235**, 116142.
62. H. Li, W. Lv, J. Xu, J. Hu and H. Liu, *J. Membr. Sci.*, 2020, **614**, 118426.
63. W. Li, J. Li, N. Wang, X. Li, Y. Zhang, Q. Ye, S. Ji and Q. -F. An, *J. Membr. Sci.*, 2020, **598**, 117671.
64. J. Li, S. Ji, G. Zhang and H. Guo, *Langmuir*, 2013, **29**, 8093-8102.
65. H. Fan, N. Wang, S. Ji, H. Yan and G. Zhang, *J. Mater. Chem. A*, 2014, **22**, 20947-20957.
66. S. Li, P. Li, D. Cai, H. Shan, J. Zhao, Z. Wang, P. Qin and T. Tan, *J. Membr. Sci.*, 2019, **579**, 141-150.
67. H. Fan, Y. Xie, J. Li, L. Zhang, Q. Zheng and G. Zhang, *J. Mater. Chem. A*, 2018, **6**, 17602-17611.
68. K. Srinivasan, K. Palanivelu and A. N. Gopalakrishnan, *Chem. Eng. Sci.*, 2007, **62**, 2905-2914.